Dual-Mode SERS-Fluorescence Immunoassay Using Graphene Quantum Dot Labeling on One-Dimensional Aligned Magnetoplasmonic Nanoparticles

Fengming Zou,[†,‡] Hongjian Zhou,[§,∥] Tran Van Tan,[§] Jeonghyo Kim,[§] Kwangnak Koh,[⊥] and Jaebeom Lee*,[§]

[†]High Magnetic Field Laboratory, Chinese Academy of Sciences, Hefei, Anhui 230031, P. R. China

[‡]Department of Nano Fusion Technology and BK21 Plus Nano Convergence Technology Division, Pusan National University, Busan 609-735, Republic of Korea

[§]Department of Cogno-Mechatronics Engineering, Pusan National University, Busan 609-735, Republic of Korea

[∥]Key Laboratory of Materials Physics, Centre for Environmental and Energy Nanomaterials, Anhui Key Laboratory of Nanomaterials and Nanotechnology, Institute of Solid State Physics, Chinese Academy of Sciences, Hefei 230031, P. R. China

[⊥]Office of General Education, Pusan National University, Busan 609-735, Republic of Korea

S Supporting Information

ABSTRACT: A novel dual-mode immunoassay based on surface-enhanced Raman scattering (SERS) and fluorescence was designed using graphene quantum dot (GQD) labels to detect a tuberculosis (TB) antigen, CFP-10, via a newly developed sensing platform of linearly aligned magneto-plasmonic (MagPlas) nanoparticles (NPs). The GQDs were excellent bilabeling materials for simultaneous Raman scattering and photo-luminescence (PL). The one-dimensional (1D) alignment of MagPlas NPs simplified the immunoassay process and enabled fast, enhanced signal transduction. With a sandwich-type immunoassay using dual-mode nanoprobes, both SERS signals and fluorescence images were recognized in a highly sensitive and selective manner with a detection limit of 0.0511 pg mL^{-1}.

KEYWORDS: graphene quantum dots, dual-mode immunoassay, surface-enhanced Raman scattering, fluorescence, biosensor, tuberculosis
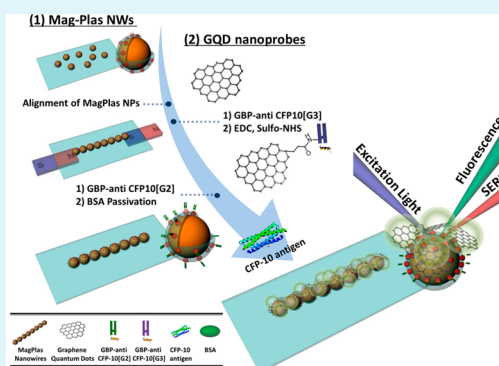
1. INTRODUCTION

Tuberculosis (TB) has a long history of being a deadly disease, and now it is still one of the world's most fatal infectious diseases in spite of the live attenuated vaccine and several antibiotics.[1] Early infection diagnosis is vital to prevent the spread of disease, and its improvement in detection is urgently required.[2] Immunoassay is an analytical method of the specific interaction between an antigen and a complementary antibody, and is widely used in biochemical analyses, clinical diagnoses, and environmental monitoring.[3] The sandwich-type immunoassay is popular since it is based on nanomaterial substrates.[4−7] Recently, multiplex immunoassays using nanomaterials have attracted significant interest.[8−12] Especially, SERS-fluorescence dual-mode nanoprobes were expected to improve the imaging quality and detection sensitivity of the fluorescence signal as quick indicator; meanwhile, SERS could help to distinguish specific targets in multiplex interactions.[13,14] Utilizing SERS-fluorescence dual-mode nanoprobes can be an extremely sensitive analytic tool in a variety of biomedical applications.

Graphene quantum dots (GQDs) are a new type of quantum dot converted from 2-dimensional graphene sheets; they are increasingly drawing the world's attention thanks to their photoluminescence (PL) and electronic properties.[15−19] Moreover, their strong quantum confinement and edge effects are advantages for electronic and optoelectronic applications.[20,21] In particular, Raman spectra of graphene have been well-studied in visible wavelengths. For example, the peak near 1580 cm^{-1}, i.e., G band, is involved in an in-plane asymmetric translational motion of two adjacent carbon atoms (E$_{2g}$ mode). The peak near 1300−1400 cm^{-1}, or the D band, is associated with the in-plane carbon ring breathing mode (A$_{1g}$ mode). The excitation wavelength determines the peak position of the D band which is the consequence of a double resonance process at the K point of the reciprocal lattice space.[22−28] The number of peak waves could be easily affected by the circumstances or

Scheme 1. Schematic Representation of the Synthesis of CFP-10 Antibody (G2 or G3)-Functionalized Fe₃O₄@PEI@Au NW (MagPlas NW) and GQD Nanocomposites and (Lower Right) the Detection Mechanism of the SERS-Induced Immunoassay To Monitor the Target CFP-10 Antigen
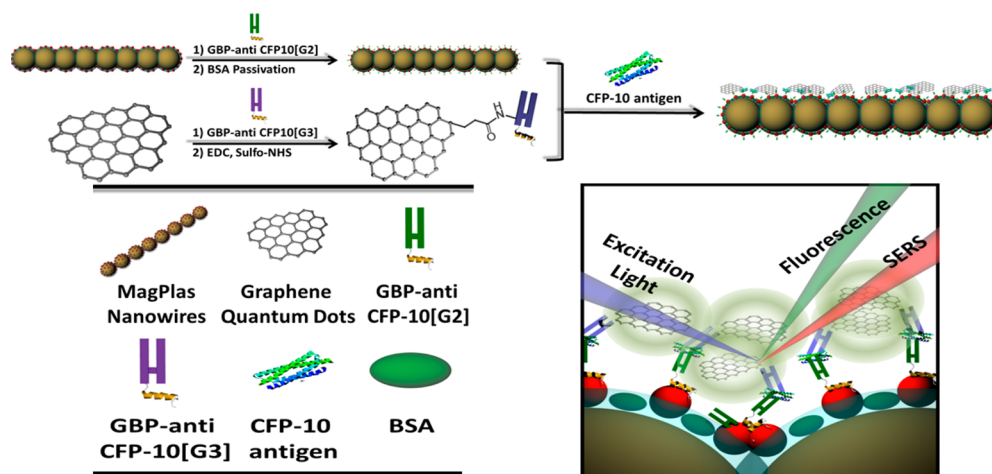
the number of layers, while the peak intensity is in proportion to the GQD concentration. In addition to the stable PL and Raman scattering, GQDs possess low cytotoxicity and high biocompatibility, both of which have been bottlenecks for biomedical applications of semiconductor QDs.[29] They can also overcome the issue of extreme aggregation that occurs in graphene sheets.[27] Therefore, GQDs can benefit future highly functional biosensor devices.

One dimensional (1D) alignments of nanoparticles (NPs) have been of interest for potential applications in electronic devices and sensing platforms. For example, in 1D-nanostructured Fe₃O₄ systems, the interplay between magnetic anisotropy and interparticle dipole–dipole interactions is the main factor determining the magnetic properties of the systems. Recently, magnetoplasmonic (Fe₃O₄@Au) core–shell NPs have been synthesized as novel hybrid nanocomposite materials, which integrate Au nanostructures with superparamagnetic Fe₃O₄ NPs to combine the plasmonic and magnetic properties in a confined cluster.[30] The Au coating on a magnetic core is expected to retain the chemical stability and biocompatibility of Au as well as the magnetic properties of the Fe₃O₄ core. Under the external static magnetic field, the Fe₃O₄@Au NPs could be self-assembled to 1D magnetoplasmonic nanochains. The successful 1D assembled nanochain is very crucial since irregular aggregated nanoparticles could hinder specific properties of assembled nanostructures, including plasmonic coupling effects, optical band gaps, and metamaterials effects. The novel metallic surface has long been considered one of the critical parameters for optimizing the metal-enhanced fluorescence (MEFs) and surface-enhanced Raman scattering (SERS). The sensitivities of MEFs and SERS are strongly dependent on the gold nanomaterials of 1D magnetoplasmonic nanochains. Therefore, 1D aligned magnetoplasmonic (MagPlas) nanowires (NWs) can be used as a new sensing material for the development of sensor platforms through MEFs and SERS technologies. Sensors made of NWs exploit some fundamental nanoscopic effects and avoid signal cross-talking for high sensitivity and selectivity.[31]

In this study, we demonstrated a proof-of-concept experiment using the Fe₃O₄–Au–GQDs nanocomplex to generate a novel surface-enhanced Raman scattering (SERS) sensor and fluorescence imaging platform for protein detection. It involves dual enhancement of Raman and fluorescence signals from GQDs by localized surface plasmon resonance (LSPR) of MagPlas NWs to achieve high sensitivity. The CFP-10 antigen was monitored using two different antibodies, referred to as G2 and G3, as follows: gold binding protein (GBP)-G3 functionalized GQDs were bound to a complementary target (CFP-10) with G2-functionalized MagPlas NWs.

2. MATERIALS AND METHODS

2.1. Materials. Polyethylenimine (PEI, branched, MW ≈ 10 000 g mol⁻¹), iron(III) chloride hexahydrate (FeCl₃·6H₂O), hydrogen tetrachloroaurate(III) trihydrate (HAuCl₄·3H₂O, 99.9%), N-ethyl-N'-(3-(dimethylamino)propyl) carbodiimide hydrochloride (EDC), N-hydroxysuccinimide (NHS), bovine serum albumin (BSA), phosphate-buffered saline (0.01 M PBS buffer solution, pH 7.4), sodium acetate anhydrous (NaAc), sodium borohydride (NaBH₄), trisodium citrate (C₆H₅Na₃O₇·3H₂O), sodium chloride (NaCl), potassium chloride (KCl), potassium phosphate monobasic (KH₂PO₄), sodium phosphate dibasic dodecahydrate (Na₂HPO₄·12H₂O), polyoxyethylene (20) sorbitan monolaurate (Tween-20), tris(hydroxymethyl) aminomethane (Tris), hydrogen chloride (HCl), sulfuric acid (H₂SO₄), nitric acid (HNO₃), sodium hydroxide (NaOH), and sodium carbonate (Na₂CO₃) were all obtained from Sigma-Aldrich (St. Louis, MO). Pitch carbon fiber (5–10 μm in diameter) was purchased from Fiber Glass Development Corporation (Brookville, OH). All chemicals were of analytical grade and were used as received with no further purification. Deionized water (Milli-Q grade, Millipore, Billerica, MA) with a resistivity of 18.2 MΩ cm⁻¹ was used in all experiments. All experiments were performed under ambient temperature.

2.2. CFP-10 Antigen and Antibodies. The recombinant CFP-10 protein and two different monoclonal antibodies against CFP-10 (G2 and G3) were prepared following previously reported methods.[7] The recombinant CFP-10 protein was expressed in *Escherichia coli* (*E. coli*) and purified according to previous methods.[32] As discussed before, Anti-CFP-10 monoclonal antibodies were selected from a pre-established scFv (single-chain variable fragment)-phage library[33,34] First, the selected scFv was expressed in Chinese hamster ovary cells. Second, monoclonal immunoglobulin G was purified by a protein column.[33,34] The preparation of GBP fusion CFP-10 (G2 and G3) has been described in detail elsewhere.[35,36] CFP-10 (G2 and G3) were used for the sandwich-type immunoassay.

2.3. Synthesis of GQD and MagPlas NP. The procedure for MagPlas NP synthesis was as follows: Fe₃O₄@PEI was prepared via the one-pot solvothermal method.[37] First, 0.68 g of FeCl₃·6H₂O was dissolved in 20 mL of ethylene glycol by ultrasonic treatment. Then, 1.8 g of NaAc and 0.5 g of PEI were added into this transparent
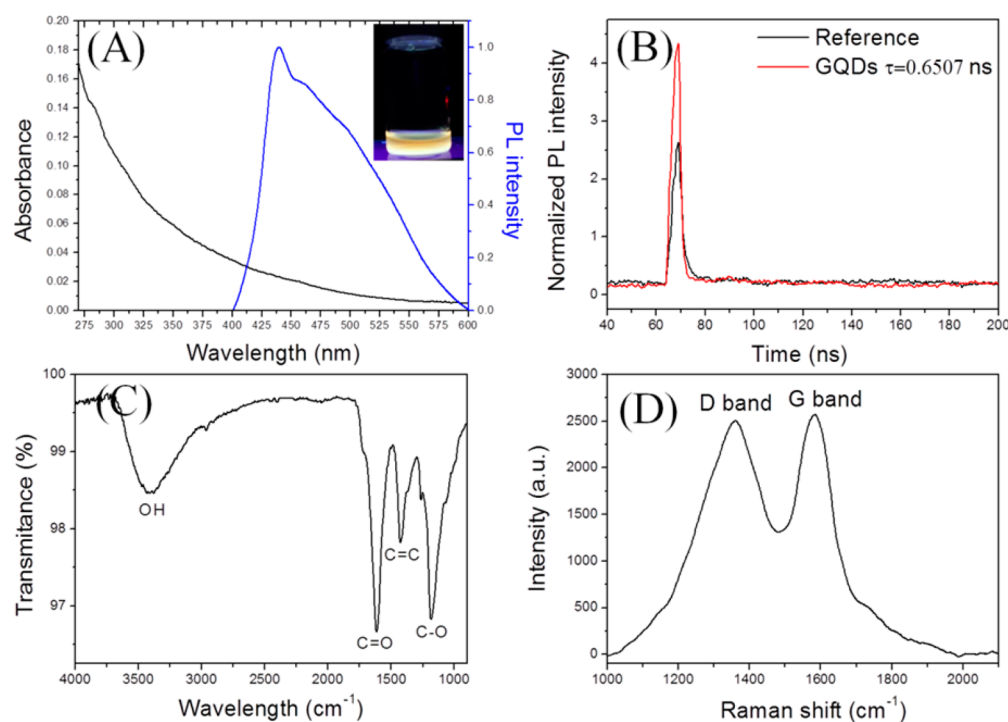
Figure 1. (A) UV and PL spectra, (B) PL lifetime, (C) FT-IR, (D) Raman spectrum of GQDs.

solution. After 20 min of strong stirring under 60 °C, the mixture was transferred into a 220 °C autoclave for 2 h. The resultant black products were rinsed with water and ethanol several times under an exterior magnet and dried in vacuum. The final products were ground to break aggregates by agate mortar. Then, Au coating was applied to the Fe_3O_4@PEI surface to produce MagPlas NPs following the strategy developed by Wang et al.[37] Fe_3O_4@PEI NPs were used as templates for Au coating by electrostatic forces. This strategy produces Fe_3O_4@PEI@Au NPs (MagPlas NPs) with a uniform size distribution. Au NPs with a diameter of 4 nm were synthesized according to the method reported by Murphy et al.[38] Then, 20 mg of the well-dried Fe_3O_4@PEI NPs was sonicated in the Au NP solution for 10 min and then mechanically stirred at room temperature for 2 h. The Fe_3O_4@PEI−Au NPs were then magnetically separated from the mixture and washed several times with water and ethanol, in turn.

GQDs were synthesized through chemical oxidation of micrometer-sized pitch-based carbon fibers (Fiber Glast Development Corporation) according to the method of Ajayan et al.[39] Further details regarding the procedure can be found in the Supporting Information.

2.4. Preparation of the Sensing Platform. The protocol for the aligned MagPlas NW immunoassay is illustrated in Scheme 1. First, a 7 μL portion of the MagPlas NPs was dropped onto microslide glasses, and an external magnetic field was engaged (1.84×10^4 Gauss, 3/4 in. × 1/10 in., disc-shaped NbFeB magnet, K&J Magnetics; Jamison, PA). After 10 min in the 55 °C oven, the glass was dry. The aligned platform was investigated using optical and electron microscopy.

2.5. Preparation of the Dual-Mode Nanoprobes. A 5 mL portion of GQDs (1 mg mL^{-1}) was first immobilized with 100 μL of G3 antibody (32 μg mL^{-1}) via the EDC/NHS bioconjugation method. Meanwhile, 10 μL of gold binding protein (GBP)-G2 antibody (0.255 mg mL^{-1}) was bound to the aligned platform of Fe_3O_4@PEI-Au NWs in 1 h at room temperature. Then, the free G2 antibody was washed twice using PBS buffer. To avoid the attachment of negatively charged GQDs to the surface of positively charged PEI@Fe_3O_4 NPs, 1% citrate was used to neutralize the PEI@Fe_3O_4 NP surface charge. Then, 20 μL of PBS buffer containing 1% BSA was used to block the nonspecific binding sites for 1 h at room temperature. After that, 10 μL of CFP-10 antigen at various concentrations (1 μg mL^{-1} to 1 pg mL^{-1}) was added to bind with G2-MagPlas NWs for 1 h, eventually providing anchor spots for G3-GQDs. Since many immuno-conjugated

structures of GQDs-G3-CFP10-G2-NWs are closely packed in the sandwich structure, many hot spots can be generated and a strong SERS-fluorescence can be obtained.

2.6. Raman Immunosensing and Fluorescence Imaging. Using 532 nm excitation (2.36 mW at the sample position), SERS spectra were recorded by Raman spectroscopy (Ramboss 500i, Dongwoo, Korea). The Rayleigh scattering light was screened by a holographic notch filter while the Raman scattering light was directly added to a charge-coupled Andor shamrock spectrograph. The laser spot diameter was 1 μm. The acquisition time was 10 s with 25 repetitions per spectrum; therefore, for each measurement, five spectra were observed for each area, on average. Fluorescence images were recorded using a fluorescence optical microscope (DM 2000, Leica, Heerbrugg, Switzerland) with a 10× microscope objective and under the excitation wavelength of 488 nm.

3. RESULTS AND DISCUSSION

3.1. Characterization of GQDs and MagPlas NPs. Graphene quantum dots are characterized with optical and electronic properties which are shaped as edge-bound nanometer-scaled graphene debris. In the previous reports, many researchers have studied the excitation-dependent emission behavior of GQDs.[40,41] Excitation-dependent PL behaviors can be widely observed in fluorescent carbon materials. Also, the excitation wavelength decides the PL color of GQDs. The initial GQDs exhibit a strong peak at 436 nm (blue emission) and a shoulder peak at 516 nm (green emission) while being excited by 320 nm wavelength light. According to previous reports, the blue emission is attributed to electron−hole recombination or quantum size effect/zig-zig effect (intrinsic state emission), while the green one is surface defects (defect state emission). Figure 1A shows the UV−vis absorption and PL spectra of GQDs. For the UV−vis spectrum of the GQDs in aqueous solution, the typical absorption peak at 290 nm could be the result of the π−π* transition of graphite sp^2 domains. The PL spectra of water-soluble GQDs were further studied under a 290 nm excitation wavelength. As shown in Figure 1A,

the PL spectrum of GQDs showed the strongest peak at 520 nm. We can observe clear yellow light when illuminated the GQD solution with 365 nm UV light (shown in the inset of Figure 1A). The luminescence decay profile of the GQDs was obtained by time-correlated single photon counting and recorded the GQD transition at 520 nm emissions excited at 380 nm (Figure 1B). The observed luminescence lifetime (τ_1) was 0.65 ns with a correction of 0.956. As shown in the FT-IR spectrum of the GQDs (Figure 1C), a strong absorption peak is centered at 1612 cm^{-1} because of the C=O stretching. The O−H bonding could be inferred from the broad peak centered at 3405 cm^{-1}, the C—O bonding from the absorption peaks at 1184 cm^{-1}, and C=C stretching from absorption peaks at 1422 cm^{-1}. The Raman spectrum (Figure 1D) can strongly prove the fragmented graphene structure of GQDs. The peaks centered at ~1579 cm^{-1} (G band) are caused by the vibration of the sp^2-bonded C atoms in a 2D hexagonal lattice, while the peak at 1358 cm^{-1} (D band) is related to scattering of disorder structure at the edges. The relative intensity of the G/D bands was ~0.91 at high concentration of GQDs, which is consistent with a previous report.[39]

Figure 2A,B shows the transmittance electron microscopy (TEM) and scanning TEM (STEM) images of the prepared
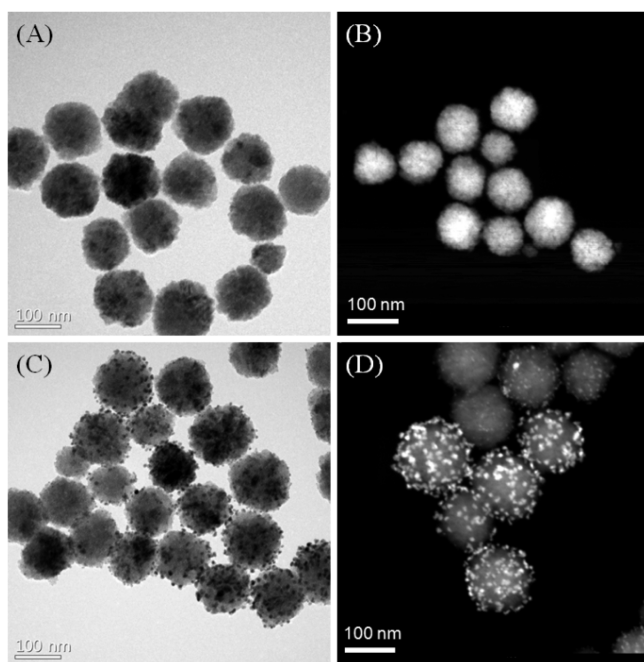

Figure 2. . TEM images of (A) Fe$_3$O$_4$@PEI NPs and (C) MagPlas NPs. STEM images of (B) Fe$_3$O$_4$@PEI NPs and (D) MagPlas NPs.

Fe$_3$O$_4$@PEI NPs. The images show that Fe$_3$O$_4$@PEI NPs were monodispersed with spherical shapes and an average diameter of 125 ± 11 nm. Au NPs for deposition were 4.17 ± 0.26 nm, as shown in Supporting Information Figure S1. The zeta potentials of Fe$_3$O$_4$@PEI NPs and Au NPs were +33 mV and −22.4 mV, respectively (Supporting Information Figure S2). Therefore, the surface of Fe$_3$O$_4$@PEI NPs can be coated with Au NPs via electrostatic interactions to produce MagPlas NPs. The TEM and STEM images of the MagPlas NPs are shown in Figure 2C,D, and Au NPs were well-dispersed on the Fe$_3$O$_4$@PEI surface. The density of the coating layer was controlled to induce optimum magnetic interactions between magnetic cores and the external magnetic field, as well as to avoid

uncontrollable agglomeration during electrostatic interactions. The assembly mechanism of MPNCs was described in our previous report.[42]

The MagPlas NPs were aligned on the glass substrate under the external magnetic field to generate a long, single chain of NWs, as shown in Figure 3. The SEM images of the aligned
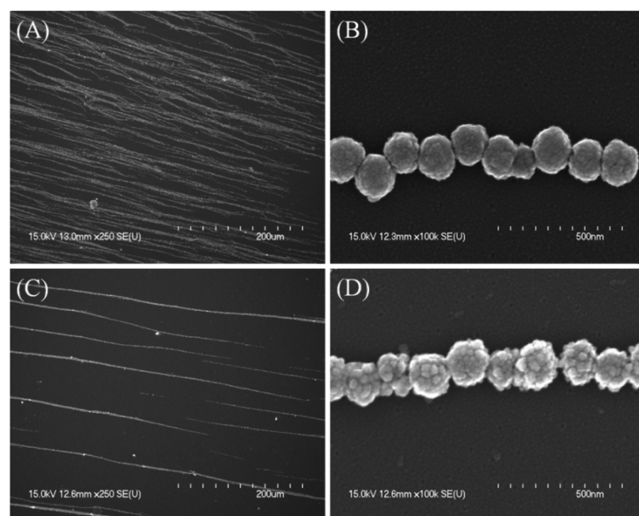
Figure 3. SEM images of Fe$_3$O$_4$ NWs (A), magnified images of Fe$_3$O$_4$ NWs (B); the SEM images of Fe$_3$O$_4$@PEI-Au NWs (C) and magnified images of Fe$_3$O$_4$@PEI-Au NWs.

NWs demonstrated that these NWs were self-assembled by single NP to a length of a few hundred micrometers and were parallel to each other in the direction of the external magnetic field flux. The rough surface of the MagPlas NWs resulted from the deposition of Au NPs on Fe$_3$O$_4$@PEI NPs, as shown in Figure 3D. In addition, we also measured the EDX spectrum of MagPlas NWs, as shown in Supporting Information Figure S8. The spectrum confirms the presence of O, Fe, and Au atoms in the MagPlas NWs.

Figure 4A,B shows the TEM images of the GQDs and G3 antibody-immobilized GQDs. Figure 4C,D shows high-resolution TEM images of Fe$_3$O$_4$@PEI NPs and the sandwich nanocomposite of the GQDs-G3-CFP10-G2-MagPlas NPs. There were many salient points on the surface of the MagPlas NPs, as shown in the comparison between parts D and C Figure 4, which were due to the immunological reaction of the GQDs-G3 antibody. Since the GBP region provides a strong and selective immobilization onto the Au(111) planes,[43] the Au NP coating is decisive in nanoprobes to ensure strong bioconjugation with a designated GBP-bound antibody as well as to provide a rough surface for further SERS and PL enhancement. Energy dispersive spectrometric elementary mapping was also conducted to examine the structure of the proposed nanoprobes (Supporting Information Figure S2). Significant signals for representative elements in the nanoprobes were detected for Au, Fe, O, and C. We can conclude that the signals of the interior nanoprobes mainly originated from the Fe$_3$O$_4$@PEI-Au NPs, while the exterior ones are from the GQDs. Thus, the fabricated nanoprobes actually possess the expected structure. Furthermore, in our experiment, 1D alignment of MagPlas NPs was carried out because the 1D assembly of MagPlas NPs induced a more closely packed geometry at the nanoscale than the NP structure did, and this
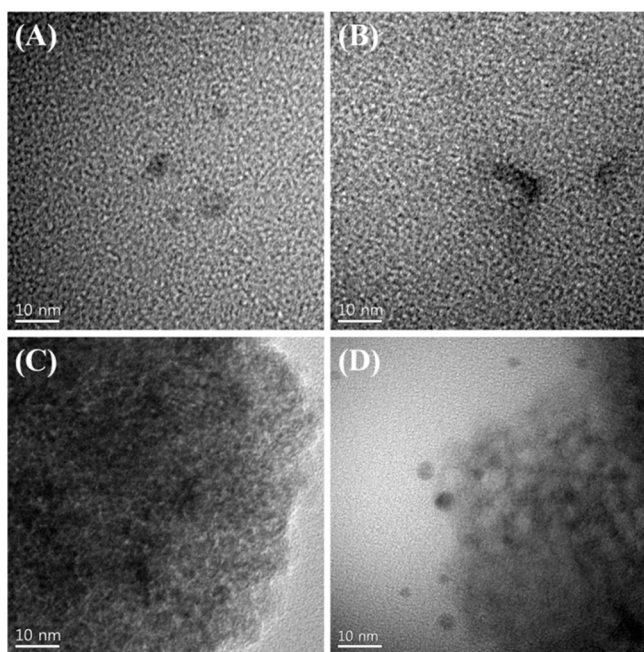
Figure 4. HRTEM images of (A) GQDs, (B) G3-modified GQDs, (C) Fe_3O_4 NPs, and (D) GQDs bound on the Fe_3O_4@Au NPs via G3-CFP10-G2 antibody sandwich structure.

property is very beneficial for further SERS and PL enhancement for sensing and imaging applications.

3.2. SERS-Fluorescence Dual-Mode Nanoprobes. The nanoprobes were able to reveal the SERS and fluorescence imaging disparity by different excitation wavelengths. With a series of properties, such as narrow emission bands and high biochemical stability and photostability, as shown in Figure 1, GQDs can be used as contrast agents for fluorescence. In our experiment, 5 mL of GQDs (1 mg mL^{-1}) was first immobilized with 100 μL of G3 antibody (32 μg mL^{-1}) via the EDC/NHS bioconjugation method. As is well-known, the EDC/NHS cross-linkers are chemical modification reagents for activating carboxyl groups for spontaneous reaction with primary amines, enabling peptide immobilization and hapten-carrier protein conjugation. The EDC/NHS cross-linkers can bond carboxyl groups of GQDs and amine groups of G3 antibody. We measured the PL spectra of GQDs and G3 modified GQDs, as shown in Supporting Information Figure S9. From our research, the unmodified GQDs can maximally absorb at 444 nm. While the slight red shift occurred at 446 nm in the PL spectra of the G3 modified GQDs, the PL spectra and intensities of G3 modified GQDs were neither broadened nor obviously weakened. Therefore, it could be asserted to be a successful bioconjugation process on the surface of GQDs with no undue aggregation. G3 conjugates with GQDs and prevents the direct region of antibodies binding each other without specific antigen. Since no such nanocomplex can be formed, no antigen will be captured by the double specific antibodies. Thus, no SERS or fluorescence signal can be detected in the platform, as shown in Supporting Information Figure S3. We are expected to get detailed antigen-related information after the immunoreactions. In our research, we have measured the SERS signals and fluorescence of the nanocomplex.

GQDs and MagPlas NP avoid the nonradiative energy transfer from the GQDs to the MagPlas NPs. However, GQDs that originate from graphene oxide sheets have unique and very

strong Raman bands that were ultimately utilized for our immunosensing experiment with a low concentration of antigens. The SERS performance of the nanoprobes was investigated. To achieve a strong enhancement effect of SERS, the MagPlas NPs were employed as SERS substrates after alignment under the external magnetic field. The GQDs-G3-CFP10-G2 antibody sandwich structure was adsorbed to the Fe_3O_4@PEI-Au NPs to generate SERS signals, enabling SERS enhancement to be monitored. The SERS spectrum for the GQDs nanoprobes excited at 532 nm is shown in Figure 1D. The GQD nanoprobes show a D band and a G band, located at 1358 and 1579 cm^{-1}, respectively. From the above experiments, we can conclude that the GQD nanoprobes are capable of distinguishing SERS and fluorescence signals under different excitation wavelengths without mixing each other up.

We also measured the SERS spectra of GQDs bound on the irregular MagPlas NPs and assembled MagPlas NWs by a G3-CFP10-G2 antibody sandwich, as shown in Supporting Information Figure S7. We can observe that the assembled MagPlas NWs exhibit the higher enhancement efficiency which is beneficial to trap and capture probing GQDs for improving the SERS performances, compared with that of irregular MagPlas NPs. It observed that the well-ordered magneto-plasmonic nanoparticles, assembled under magnetic force, exhibit a surface plasmon resonance (SPR) property which could build a strong local electric field which can promote Raman activity in vibrational modes. Therefore, the 1D-assembled MagPlas NWs are chosen as substrate in the current experiment.

3.3. Immunoassay. The sandwich-type assays were performed to validate the immunoassay protocol of multiplex biodetection. The immune protocol was carried out following Scheme 1. The MagPlas NPs were aligned on the surfaces of silicon wafers under the external magnetic field. Then, antibodies were fixed on the surfaces of the MagPlas NPs and GQDs. So the sandwich-type nanocomplex with the target antigen (CFP10) was created. The nanocomplex is shown in Scheme 1. Briefly, the CFP-10 antigen is captured by the sandwich structure via the antibody—antigen interaction, and the MagPlas NWs show SERS and fluorescence signals that match.
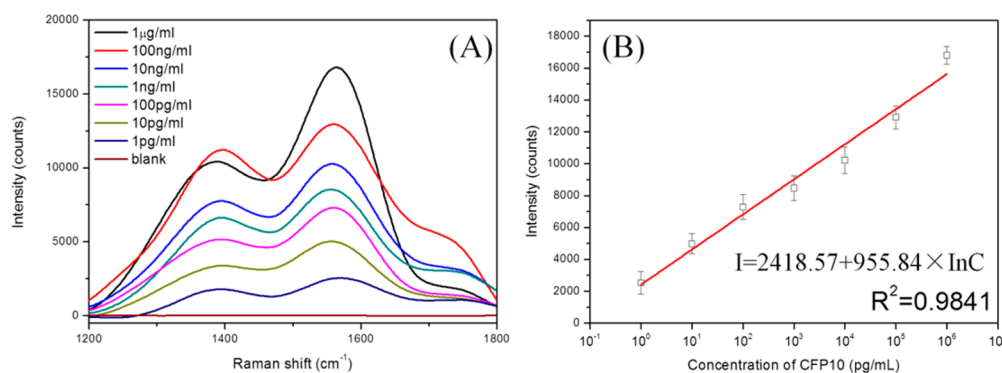
In our experiments, CFP-10 antigen was used as the target molecule for the proof-of-concept experiment. The MagPlas NPs were immobilized with GBP-G2 antibody, while the GQDs were immobilized with G3 antibody. The nonspecific binding sites on the surfaces of MagPlas NWs were blocked by BSA. First, the specificity of the immunoassay protocol was examined. A 10 μL portion of 10 pg mL^{-1} CFP-10 antigen and pure PBS solution were added to the mixtures divided into two groups but both containing G3-modified GQD antibody and GBP-G2-modified MagPlas NWs. The immunoreaction proceeded for 2 h. Then we detected SERS and fluorescence signals of the nanocomplex. As expected, there is no trace of strong SERS signals until CFP-10 antigen molecules were added. Because the specific antigens help form the sandwich-type nanocomplexes, there are more particles in the corresponding platform than otherwise. The SERS spectra from two sets of solutions were, respectively, measured as shown in Supporting Information Figure S3. It was not hard to find that the nanocomplex with specific antigens send out stronger SERS signals than those with no specific antigen. Fluorescence images of the nanocomplex are shown in Figure 5. In the bright field, parts A and C of Figure 5 show the

Bright field   Fluorescence
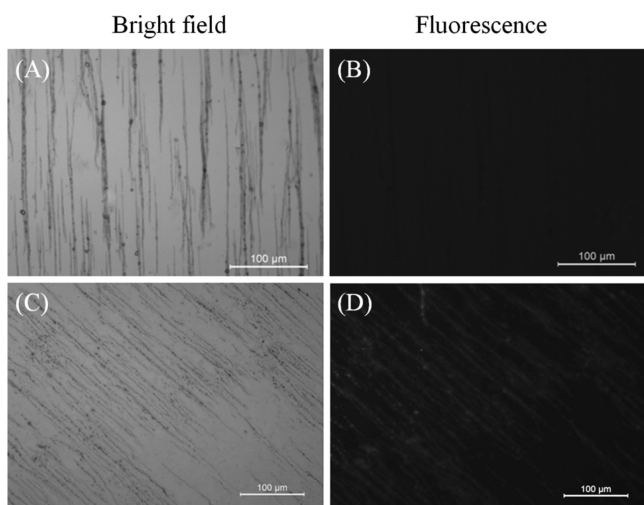
Figure 5. Fluorescence optical images of Fe$_3$O$_4$@PEI-Au NWs (A, B) and GQDs-G3-CFP10-G2 antibody sandwich structure on the surface of Fe$_3$O$_4$@PEI-Au NWs (C, D). Bright field (left) and fluorescence (right) images.

MagPlas NWs without and with antigen binding. In the fluorescence images, however, only Figure 5D shows the green fluorescence indicating NWs owing to GQDs immobilized on the surface of Fe$_3$O$_4$@PEI-Au NWs. This series of research shows that target antigens could be easily detected in such an immunoassay system. Thus, the immunoassay protocol can be used to specifically detect target biomolecules in a solid platform.

Next, CFP-10 antigen was responsible for detecting the sensitivity of the exhibited immunoassay protocol as the model target biomolecules. Various concentrations of CFP-10 antigen (1 μg mL^{-1} to 1 pg mL^{-1}) were added to 8 sets of GBP-G2-supplemented Fe$_3$O$_4$@PEI-Au NPs and G3-modified GQDs solutions. One additional set of solutions was added with pure PBS solution as blank control. After 2 h of immunoreaction, each nanocomplex set was collected and measured by Raman spectroscopy. The precipitates of each solution enabled us to catch the SERS spectrum of the 1579 cm^{-1} peak (as demonstrated in Figure 6A). This result indicated that the concentration of CFP-10 antigen is in proport to the SERS spectra. Figure 6B shows a plot of the intensity of the 1579 cm^{-1} peak against the logarithm of the CFP-10 antigen concentration, clearly revealing the decrease in SERS intensity.

For the SERS signals, a good linear response was achieved within the range of 1 pg mL^{-1} to 1 μg mL^{-1} CFP-10 antigen. The definition of detection limitation in this research is that the signal of the analyte concentration was 3 times stronger than that in the blank control and its value was 0.0511 pg mL^{-1} for the immunoassay.[44] The above-mentioned results proved that the immunoassay protocol can be used to realize highly sensitive and selective multiplex detection of target molecules. In addition, one peak at 1750 cm^{-1} was clearly observed in Figure 6A. According to the previous report, we attribute the peak of 1750 cm^{-1} to the M band due to the intravalley double resonance scattering process of bilayer graphene and a few layers of graphene. Similar to the G′ mode, the evolution of this M band coupled with the increasing number of graphene layers could be inflicted by that of electronic band with graphene films structure.[45]

Note that the ratio of intensity of D/G bands is a measure of the defects present on graphene structure.[46] In-plane vibrations of sp^2 bonded carbon atoms create the G band whereas the D band is the result of out of plane vibrations attributed to the presence of structural defects.[47] If the D band is higher, it indicates that the sp^2 bonds are broken which in turn means that there are more sp^2 bonds. Figure 6 shows that G bands of GQDs were more enhanced than that of the D band. The GQDs bind to the surface of the MagPlas NW G3-CFP10-G2 antibody sandwich in the immunoassay. This results in increasing sp^2 bonds (G band) but did not break the sp^2 bonds (D band). Moreover, some GQDs overlapped with each other in the immunoassay, inevitably. Thus, the M band shows weak enhancement in the peak of 1750 cm^{-1}.

This new immunoassay protocol has several advantages relative to previous methods. The Fe$_3$O$_4$@PEI-Au NWs allow the detection to be performed on a solid platform, thus greatly simplifying the immunoassay process. It also has great multiplexing ability owing to the dual-mode nanoprobes because it eliminates the need to employ multiple SERS reporters or fluorescence semiconductor QDs with different emission wavelengths. GQDs can generate both SERS and fluorescence signals simultaneously. Moreover, the fluorescence signal is a fast qualitative indicator of the immunoreaction, and the SERS signal can be used for the quantitative identification of the specific target molecules.

Figure 6. (A) Concentration-dependent SERS spectra of the 1579 cm^{-1} peak obtained from the precipitates corresponding to different concentrations of CFP-10 antigen. (B) SERS intensity for the 1579 cm^{-1} peak plotted against the logarithm of CFP-10 antigen concentrations ranging from 1 pg mL^{-1} to 1 μg mL^{-1}. The error bars represent the standard deviation of 5 measurements.

4. CONCLUSIONS

The study of SERS and fluorescence signals helps us build a brand new immunoassay protocol. Specifically, in the dual-mode nanoprobes, the 1D aligned MagPlas NWs serve as the SERS substrate, and water-soluble GQDs was the fluorescent indicator and Raman signal. With such a structure, dual-mode nanoprobes can be used to detect SERS and fluorescence signals to monitor immunoreaction results. The biomolecules were characterized with high sensitivity, and selective recognition on a solid platform with a detection limit of 0.0511 pg mL^{-1} was created. Thanks to the easy operation and superior multiplexing ability (attributed to the dual-mode nanoprobes) of the immunoassay protocol, this is expected to be further applied in high throughput screening of target molecules.

■ ASSOCIATED CONTENT

Ⓢ Supporting Information

Additional synthesis process of GQDs, size distribution, zeta potential, STEM images and EDX elementary mapping, SERS spectra, fluorescence optical images, EDX spectrum, PL spectra, and magnetization moments estimated for Fe_3O_4@PEI NPs. The Supporting Information is available free of charge on the ACS Publications website at DOI: 10.1021/acsami.5b02523.

■ AUTHOR INFORMATION

Corresponding Author

*E-mail: jaebeom@pusan.ac.kr. Phone: (+82)55-350-5298. Fax: (+82)55-350-5299.

Notes

The authors declare no competing financial interest.

■ ACKNOWLEDGMENTS

■ REFERENCES

(1) Smith, I. Mycobacterium Tuberculosis Pathogenesis and Molecular Determinants of Virulence. *Clin. Microbiol. Rev.* **2003**, *16*, 463−496.

(2) Van Pinxteren, L. A.; Ravn, P.; Agger, E. M.; Pollock, J.; Andersen, P. Diagnosis of Tuberculosis Based on the Two Specific Antigens ESAT-6 and CFP10. *Clin. Diagn. Lab. Immunol.* **2000**, *7*, 155−160.

(3) Wu, L.; Wang, Z.; Zong, S.; Huang, Z.; Zhang, P.; Cui, Y. A SERS-Based Immunoassay with Highly Increased Sensitivity Using Gold/Silver Core-Shell Nanorods. *Biosens. Bioelectron.* **2012**, *38*, 94−99.

(4) Zong, S.; Wang, Z.; Zhang, R.; Wang, C.; Xu, S.; Cui, Y. A Multiplex and Straightforward Aqueous Phase Immunoassay Protocol through the Combination of SERS-fluorescence Dual Mode Nanoprobes and Magnetic Nanobeads. *Biosens. Bioelectron.* **2013**, *41*, 745−751.

(5) Zhou, H.; Lee, J.; Park, T. J.; Lee, S. J.; Park, J. Y.; Lee, J. Ultrasensitive DNA Monitoring by Au−Fe₃O₄ Nanocomplex. *Sens. Actuators, B* **2012**, *163*, 224−232.

(6) Zhou, H.; Dong, J.; Deo, V. K.; Park, E. Y.; Lee, J. Detection of Anti-Neospora Antibodies in Bovine Serum by Using Spiky Au−CdTe Nanocomplexes. *Sens. Actuators, B* **2013**, *178*, 192−199.

(7) Kim, J.; Lee, J.; Lee, K. I.; Park, T. J.; Kim, H. J.; Lee, J. Rapid Monitoring of CFP-10 During Culture of Mycobacterium tuberculosis by Using a Magnetophoretic Immunoassay. *Sens. Actuators, B* **2013**, *177*, 327−333.

(8) Fu, Q.; Zhu, J.; Van Eyk, J. E. Comparison of Multiplex Immunoassay Platforms. *Clin. Chem.* **2010**, *56*, 314−318.

(9) Zong, C.; Wu, J.; Xu, J.; Ju, H.; Yan, F. Multilayer Hemin/G-Quadruplex Wrapped Gold Nanoparticles as Tag for Ultrasensitive Multiplex Immunoassay by Chemiluminescence Imaging. *Biosens. Bioelectron.* **2013**, *43*, 372−378.

(10) Han, K. C.; Yang, E. G.; Ahn, D. R. A Highly Sensitive, Multiplex Immunoassay Using Gold Nanoparticle-Enhanced Signal Amplification. *Chem. Commun.* **2012**, *48*, 5895−5897.

(11) Han, S. W.; Jang, E.; Koh, W. G. Microfluidic-based Multiplex Immunoassay System Integrated with an Array of QD-Encoded Microbeads. *Sens. Actuators, B* **2015**, *209*, 242−251.

(12) Jeong, M. S.; Ahn, D. R. A Microwell Plate-based Multiplex Immunoassay for Simultaneous Quantitation of Antibodies to Infectious Viruses. *Analyst* **2015**, *140*, 1995−2000.

(13) Niu, X.; Chen, H.; Wang, Y.; Wang, W.; Sun, X.; Chen, L. Upconversion Fluorescence-SERS Dual-Mode Tags for Cellular and In Vivo Imaging. *ACS Appl. Mater. Interfaces* **2014**, *6*, 5152−5160.

(14) Wang, Z.; Zong, S.; Li, W.; Wang, C.; Xu, S.; Chen, H.; Cui, Y. SERS-Fluorescence Joint Spectral Encoding Using Organic−Metal-QD Hybrid Nanoparticles with a Huge Encoding Capacity for High-Throughput Biodetection: Putting Theory into Practice. *J. Am. Chem. Soc.* **2012**, *134*, 2993−3000.

(15) Luk, C. M.; Tang, L. B.; Zhang, W. F.; Yu, S. F.; Teng, K. S.; Lau, S. P. An Efficient and Stable Fluorescent Graphene Quantum Dot−Agar Composite as a Converting Material in White Light Emitting Diodes. *J. Mater. Chem.* **2012**, *22*, 22378−22381.

(16) Yan, X.; Cui, X.; Li, L. s. Synthesis of Large, Stable Colloidal Graphene Quantum Dots with Tunable Size. *J. Am. Chem. Soc.* **2010**, *132*, 5944−5945.

(17) Shi, H.; Barnard, A. S.; Snook, I. K. Quantum Mechanical Properties of Graphene Nano-Flakes and Quantum Dots. *Nanoscale* **2012**, *4*, 6761−6767.

(18) Ritter, K. A.; Lyding, J. W. The Influence of Edge Structure on the Electronic Properties of Graphene Quantum Dots and Nanoribbons. *Nat. Mater.* **2009**, *8*, 235−242.

(19) Sun, H.; Wu, L.; Gao, N.; Ren, J.; Qu, X. Improvement of Photoluminescence of Graphene Quantum Dots with a Biocompatible Photochemical Reduction Pathway and Its Bioimaging Application. *ACS Appl. Mater. Interfaces* **2013**, *5*, 1174−1179.

(20) Lu, Q.; Huang, R. Nonlinear Mechanics of Single-Atomic-Layer Graphene Sheets. *Int. J. Appl. Mech. Eng.* **2009**, *1*, 443−467.

(21) Yang, Z.; Gao, R.; Hu, N.; Chai, J.; Cheng, Y.; Zhang, L.; Wei, H.; Kong, E.; Zhang, Y. The ProspectiveTwo-Dimensional Graphene Nanosheets: Preparation, Functionalization, and Applications. *Nano-Micro Lett.* **2012**, *4*, 1−9.

(22) Tuinstra, F.; Koenig, J. L. Raman Spectrum of Graphite. *J. Chem. Phys.* **1970**, *53*, 1126−1130.

(23) Reich, S.; Thomsen, C. Raman Spectroscopy of Graphite. *Philos. Trans. R. Soc., A* **2004**, *362*, 2271−2288.

(24) Thomsen, C.; Reich, S. Double Resonant Raman Scattering in Graphite. *Phys. Rev. Lett.* **2000**, *85*, 5214.

(25) Saito, R.; Jorio, A.; Souza Filho, A. G.; Dresselhaus, G.; Dresselhaus, M. S.; Pimenta, M. A. Probing Phonon Dispersion Relations of Graphite by Double Resonance Raman Scattering. *Phys. Rev. Lett.* **2001**, *88*, 027401.

(26) Casiraghi, C.; Hartschuh, A.; Qian, H.; Piscanec, S.; Georgi, C.; Fasoli, A.; Novoselov, K. S.; Basko, D. M.; Ferrari, A. C. Raman Spectroscopy of Graphene Edges. *Nano Lett.* **2009**, *9*, 1433−1441.

(27) Park, J. S.; Reina, A.; Saito, R.; Kong, J.; Dresselhaus, G.; Dresselhaus, M. S. G Band Raman Spectra of Single, Double and Triple Layer Graphene. *Carbon* **2009**, *47*, 1303−1310.

(28) Ferrari, A. C.; Meyer, J. C.; Scardaci, V.; Casiraghi, C.; Lazzeri, M.; Mauri, F.; Piscanec, S.; Jiang, D.; Novoselov, K. S.; Roth, S. Raman

Spectrum of Graphene and Graphene Layers. *Phys. Rev. Lett.* **2006**, *97*, 187401.

(29) Zhu, S.; Zhang, J.; Qiao, C.; Tang, S.; Li, Y.; Yuan, W.; Li, B.; Tian, L.; Liu, F.; Hu, R. Strongly Green-Photoluminescent Graphene Quantum Dots for Bioimaging Applications. *Chem. Commun.* **2011**, *47*, 6858−6860.

(30) Zhou, H.; Kim, J. P.; Bahng, J. H.; Kotov, N. A.; Lee, J. Self−Assembly Mechanism of Spiky Magnetoplasmonic Supraparticles. *Adv. Funct. Mater.* **2014**, *24*, 1439−1448.

(31) Tran, V. T.; Zhou, H.; Kim, S.; Lee, J.; Kim, J.; Zou, F.; Kim, J.; Park, J.; Lee, J. Self-Assembled Magnetoplasmonic Nanochain for DNA Sensing. *Sens. Actuators, B* **2014**, *203*, 817−823.

(32) Shin, A. R.; Shin, S. J.; Lee, K. S.; Eom, S. H.; Lee, S. S.; Lee, B. S.; Lee, J. S.; Cho, S. N.; Kim, H. J. Improved Sensitivity of Diagnosis of Tuberculosis in Patients in Korea via a Cocktail Enzyme-Linked Immunosorbent Assay Containing the Abundantly Expressed Antigens of the K Strain of Mycobacterium tuberculosis. *Clin. Vaccine Immunol.* **2008**, *15*, 1788−1795.

(33) Hong, S. C.; Chen, H.; Lee, J.; Park, H. K.; Kim, Y. S.; Shin, H. C.; Kim, C. M.; Park, T. J.; Lee, S. J.; Koh, K. Ultrasensitive Immunosensing of Tuberculosis CFP-10 Based on SPR Spectroscopy. *Sens. Actuators, B* **2011**, *156*, 271−275.

(34) Hong, S. C.; Lee, J.; Shin, H. C.; Kim, C. M.; Park, J. Y.; Koh, K.; Kim, H. J.; Chang, C. L.; Lee, J. Clinical Immunosensing of Tuberculosis CFP-10 in Patient Urine by Surface Plasmon Resonance Spectroscopy. *Sens. Actuators, B* **2011**, *160*, 1434−1438.

(35) Lee, J.; Kim, J.; Ahmed, S. R.; Zhou, H.; Kim, J. M.; Lee, J. Plasmon-Induced Photoluminescence Immunoassay for Tuberculosis Monitoring Using Gold-Nanoparticle-Decorated Graphene. *ACS Appl. Mater. Interfaces* **2014**, *6*, 21380−21388.

(36) Kim, J.; Hong, S. C.; Hong, J. C.; Chang, C. L.; Park, T. J.; Kim, H. J.; Lee, J. Clinical Immunosensing of Tuberculosis CFP-10 Antigen in Urine Using Interferometric Optical Fiber Array. *Sens. Actuators, B* **2015**, DOI: 10.1016/j.snb.2015.04.046.

(37) Wang, Y.; Xu, F.; Zhang, L.; Wei, X. One-Pot Solvothermal Synthesis of Fe_3O_4−PEI Composite and Its Further Modification with Au Nanoparticles. *J. Nanopart. Res.* **2013**, *15*, 1−11.

(38) Jana, N. R.; Gearheart, L.; Murphy, C. J. Seeding Growth for Size Control of 5−40 nm Diameter Gold Nanoparticles. *Langmuir* **2001**, *17*, 6782−6786.

(39) Peng, J.; Gao, W.; Gupta, B. K.; Liu, Z.; Romero-Aburto, R.; Ge, L.; Song, L.; Alemany, L. B.; Zhan, X.; Gao, G. Graphene Quantum Dots Derived from Carbon Fibers. *Nano Lett.* **2012**, *12*, 844−849.

(40) Zhu, S.; Zhang, J.; Tang, S.; Qiao, C.; Wang, L.; Wang, H.; Liu, X.; Li, B.; Li, Y.; Yu, W. Surface Chemistry Routes to Modulate the Photoluminescence of Graphene Quantum Dots: From Fluorescence Mechanism to Up−Conversion Bioimaging Applications. *Adv. Funct. Mater.* **2012**, *22*, 4732−4740.

(41) Zhu, S.; Zhang, J.; Liu, X.; Li, B.; Wang, X.; Tang, S.; Meng, Q.; Li, Y.; Shi, C.; Hu, R. Graphene Guantum Dots with Controllable Surface Oxidation, Tunable Fluorescence and Up-Conversion Emission. *RSC Adv.* **2012**, *2*, 2717−2720.

(42) Tran, V. T.; Zhou, H.; Lee, S.; Hong, S. C.; Kim, J.; Jeong, S. Y.; Lee, J. Magnetic-Assembly Mechanism of Superparamagneto-Plasmonic Nanoparticles on a Charged Surface. *ACS Appl. Mater. Interfaces* **2015**, *7*, 8650−8658.

(43) So, C. R.; Kulp, J. L.; Oren, E. E.; Zareie, H.; Tamerler, C.; Evans, J. S.; Sarikaya, M. Molecular Recognition and Supramolecular Self-Assembly of a Genetically Engineered Gold Binding Peptide on Au{111}. *ACS Nano* **2009**, *3*, 1525−1531.

(44) Apostol, I.; Miller, K. J.; Ratto, J.; Kelner, D. N. Comparison of Different Approaches for Evaluation of the Detection and Quantitation Limits of a Purity Method: A Case Study Using a Capillary Isoelectrofocusing Method for a Monoclonal Antibody. *Anal. Biochem.* **2009**, *385*, 101−106.

(45) Cong, C.; Yu, T.; Saito, R.; Dresselhaus, G. F.; Dresselhaus, M. S. Second-Order Overtone and Combination Raman Modes of Graphene Layers in the Range of 1690−2150 cm−1. *ACS Nano* **2011**, *5*, 1600−1605.

(46) Lalwani, G.; Xing, W.; Sitharaman, B. Enzymatic Degradation of Oxidized and Reduced Graphene Nanoribbons by Lignin Peroxidase. *J. Mater. Chem. B* **2014**, *2*, 6354−6362.

(47) Kudin, K. N.; Ozbas, B.; Schniepp, H. C.; Prud'Homme, R. K.; Aksay, I. A.; Car, R. Raman Spectra of Graphite Oxide and Functionalized Graphene Sheets. *Nano Lett.* **2008**, *8*, 36−41.